Directed nucleation and growth by balancing local supersaturation and substrate/nucleus lattice mismatch

Li, L.; Fijneman, A.J.; Kaandorp, J.A.; Aizenberg, J.; Noorduin, W.L.

Published in:
Proceedings of the National Academy of Sciences of the United States of America

DOI:
10.1073/pnas.1712911115

Published: 03/04/2018

Document Version
Accepted manuscript including changes made at the peer-review stage

Directed nucleation and growth by balancing local supersaturation and substrate/nucleus lattice mismatch

L. Li,[1,2,3] A. J. Fijneman,[1,4] J. A. Kaandorp,[5] J. Aizenberg,[1,2,6,7] W. L. Noorduin,[1,8]

[1]John A. Paulson School of Engineering and Applied Sciences, Harvard University, Cambridge, MA 02138, USA
[2]Wyss Institute for Biologically Inspired Engineering, Harvard University, Boston, MA 02115, USA
[3]Department of Mechanical Engineering, Virginia Polytechnic Institute and State University, Blacksburg, VA 24060, USA
[4]Department of Chemical Engineering and Chemistry, Eindhoven University of Technology, 5612 AZ Eindhoven, The Netherlands
[5]Computational Science Lab, Faculty of Science, University of Amsterdam, 1098 XH Amsterdam, The Netherlands
[6]Kavli Institute for Bionano Science and Technology, Harvard University, Cambridge, MA 02138, USA
[7]Department of Chemistry and Chemical Biology, Harvard University, Cambridge, MA 02138, USA
[8]AMOLF, 1098 XG Amsterdam, The Netherlands.

Controlling nucleation and growth is crucial in biological and artificial mineralization and self-assembly processes. The nucleation barrier is determined by the interfaces and local supersaturation. Although chemically tailored substrates and lattice mismatches are routinely used to modify various forms of energy contributions as resulted from the substrate/nucleus interface and thereby steer controlled heterogeneous nucleation, strategies to combine this with control over local supersaturations have remained virtually unexplored. Here we demonstrate simultaneous control over both parameters to direct the positioning and growth direction of mineralizing compounds on preselected polymorphic substrates. We exploit the polymorphic nature of calcium carbonate ($CaCO_3$) to locally manipulate the carbonate concentration and lattice mismatch between the nucleus and substrate, such that barium carbonate ($BaCO_3$) and strontium carbonate ($SrCO_3$) nucleate only on specific $CaCO_3$ polymorphs. Based on this approach we position different materials and shapes on predetermined $CaCO_3$ polymorphs in sequential steps, and guide the growth direction using locally created supersaturations. These results shed light on nature's remarkable mineralization capabilities and outline new fabrication strategies for advanced materials, such as ceramics, photonic structures and semiconductors.

Significance

The energy barrier for a classical heterogeneous crystal nucleation can be controlled by the energy contributions from the substrate/nucleus interface and local supersaturation. Exerting control over crystal growth thus requires modifying either one of these terms. We here introduce a strategy to modulate the contributions of *both* parameters simultaneously using substrates containing different crystal structures of calcium carbonate. Based on a theoretical analysis, we program both the positioning and growth direction of carbonate salts on preselected polymorphs. These findings may hold relevance for understanding, mimicking and ultimately expanding upon nature's mineralization strategies and for developing functional microscale materials.

Introduction

Spurred by the recent advancement in techniques such as microfabrication and electron microscopy, there has been tremendous advancement in understanding and controlling both

biological and artificial mineralization processes (1-4). Unlike homogeneous nucleation, heterogeneous nucleation allows for an effective strategy to control the local nucleation energy barrier by modifying the chemical and structural characteristics between the nascent nucleus and substrates (5-12). Alternatively, a local increase of the supersaturation can onset nucleation (13-15) – an approach broadly utilized by natural systems through ion channels that deliver crystallizing components to the specific site where nucleation should occur, – but this approach has hardly been explored in artificial systems. Only recently, such local supersaturations were created using an ion binding biomimetic matrix (4). However, little or no work has been done to develop principles that allow for simultaneous control over the local supersaturation and interfacial free energy for directing the nucleation position, let alone the growth (15).

While virtually all previous studies have been aimed at avoiding polymorphism (16), we here use the ability of compounds to organize in different crystal forms to rationally control local supersaturations in the vicinities of different polymorphs and subtle variations in the lattice mismatch between the substrate and the nucleus. An ideal model system to test this strategy is the crystallization of $BaCO_3$ selectively on top of different polymorphs of $CaCO_3$. $CaCO_3$ is the most abundant biomineral and can be found in three anhydrous polymorphs that all occur in living organisms (17-23). At room temperature calcite is the most stable polymorph, followed by aragonite and finally vaterite as the least stable structure. To demonstrate the ability to tune the positioning of $BaCO_3$ on top of these polymorphs and its growth direction, we analyze and exploit local variations of supersaturations induced by the difference in the dissolution rate of $CaCO_3$ polymorphs. Additionally, the crystal structures of calcite, aragonite, and vaterite are different from each other, and only aragonite resembles that of $BaCO_3$ (23). This variation in crystal structures allows for direct evaluation of the effects of the lattice mismatch on templated nucleation of $BaCO_3$ on selected $CaCO_3$ polymorphs modulated by the local supersaturation gradients.

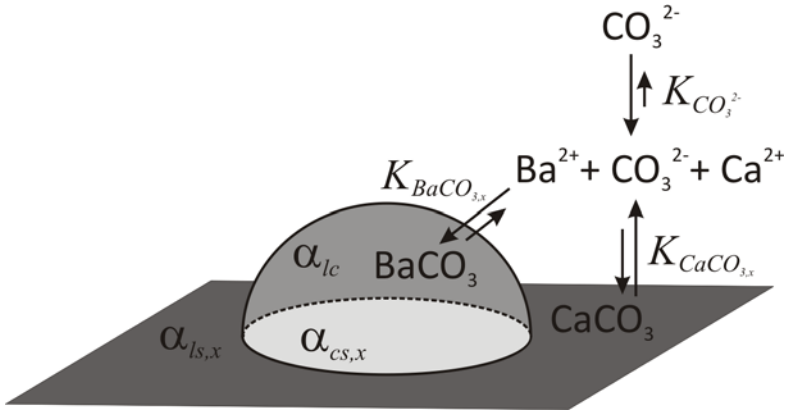

Fig. 1. Nucleation of $BaCO_3$ on a $CaCO_3$ substrate. The energy barrier for nucleation is determined by (i) the contributions of the interfacial free energies arising from the lattice mismatch between liquid-crystal α_{lc}, liquid-substrate $\alpha_{ls,x}$ and substrate-crystal $\alpha_{cs,x}$, and (ii) the local supersaturation, which depends on the concentration of ions in the solution, the influx of CO_3^{2-}, the crystallization rate of $BaCO_3$ and dissolution rate of $CaCO_3$, k_{BaCO3} and $k_{CaCO3,x}$ respectively for a specific crystal structure *x*. By controlling the influx of the CO_3^{2-}, the balance can be shifted from the major contribution from the lattice mismatch at high $[CO_3^{2-}]_{bulk}$ to a local supersaturation-dominated process controlled by the differences in the solubility of $CaCO_3$ polymorphs at low $[CO_3^{2-}]_{bulk}$. Note that the hemispherical representation is chosen for illustrative purposes and will depend on the specific nucleation conditions.

Results and Discussions

To understand the unique interplay between the interfacial free energy that arises from the lattice mismatch and supersaturation in this system, we analyze a solution containing Ba^{2+} ions in which an influx of CO_3^{2-} causes the templated nucleation of $BaCO_3$ on a $CaCO_3$ substrate with crystal structure *x* (Fig. 1). According to classical nucleation theory (13-15), the energy barrier to form a critical nucleus, Δg_n, can be described as a function of the local supersaturation σ and the interfacial free energy α according to

$$\Delta g_n \propto \frac{\alpha_x{}^3}{\sigma_x{}^2} \quad . \tag{1}$$

The lattice mismatch between the $BaCO_3$ nucleus and the underlying substrate directly contributes to the interfacial energy penalties, which include an energy contribution due to the difference in chemical bonding, and a strain energy contribution from the interface and the nucleate volume that arises from the incoherent ordering at the interface. Although analytical expressions of each energy contribution are hard to achieve due to the complexity of the system, both energy contributions should decrease as the substrate/nucleus interface becomes more crystallographically aligned and coherent.

The energy gain resulting from the chemical potential energy is directly related to the supersaturation of $BaCO_3$. In case the substrate has a higher solubility than the nucleating compound, and the rate of dissolution of the substrate is higher than the rate of growth of the nucleating crystal (Fig. 1), the supersaturation in $BaCO_3$ can be expressed as:

$$\sigma = \ln\left(\frac{k_{BaCO_3}[Ba^{2+}][CO_3^{2-}]_{bulk}}{k_{BaCO_3}[Ba^{2+}] - k_x + k_x{}'[Ca^{2+}]_s} \right) \tag{2}$$

with k_{BaCO_3} the crystallization rate constant of $BaCO_3$, $[CO_3^{2-}]_{bulk}$ the concentration of carbonate in the bulk solution, $[Ca^{2+}]_s$ the Ca^{2+} concentration close to the surface of the $CaCO_3$ crystal, k_x the dissolution rate constant of $CaCO_3$ for a specific polymorph *x*, and $k_x' = k_{CaCO_3,x} / K_{sp\_CaCO_3,x}$ where $K_{sp\_CaCO_3,x}$ is the solubility product of a specific polymorph *x* of $CaCO_3$ (see SI, 24-27). We assume $k_{vaterite} > k_{aragonite} > k_{calcite}$ and $K_{sp,vaterite} > K_{sp,aragonite} > K_{sp,calcite}$, which implies that both the dissolution rate and solubility of vaterite is higher than those for aragonite and calcite. In case of ample availability of Ba^{2+}, the free energy barrier Δg_n for nucleation on a specific polymorph of $CaCO_3$ is controlled by the interplay of: (a) the concentration of carbonate from the bulk solution, (b) the polymorph-dependent lattice mismatch of the $CaCO_3$ substrate, and (c) the substrate solubility equilibrium. We therefore expect that the choice of the positioning of the nucleation can be tuned by the subtle changes in relative contributions of these parameters. Below we consider various scenarios where the impact of these parameters is analyzed and exploited to direct the nucleation and growth of $BaCO_3$.

To evaluate the effects of lattice mismatch in the carbonate system studied here, we characterized the crystallographic relationships of $BaCO_3$ grown on top of calcite, aragonite and vaterite as substrate crystals. The overgrown $BaCO_3$ crystals can be easily differentiated from the underlying $CaCO_3$ crystals in backscatter electron microscopy due to their electron density difference (Fig. 2A, i, ii). Through focused ion beam (FIB) milling, electron-transparent transmission electron microscopy (TEM) samples were prepared at the interfaces of nucleus and substrates, from which the morphological and crystallographic characteristics were evaluated (Fig. 2A, iii-v). $BaCO_3$ exhibit well alignment with calcite and aragonite by sharing the same *c*-axes, while vaterite showed no crystallographic alignment (Fig. 2A; see Supplementary Information). This lack of orientation matching thus indicates a higher interfacial free energy for nucleation on vaterite as

compared to calcite and aragonite. A qualitative estimation of the lattice mismatch shows that $BaCO_3$ has a slightly smaller lattice mismatch in both ***a*** and ***b*** directions on calcite as the substrate in comparison to aragonite as the substrate (SI, section 8) (12). Therefore, when all three polymorphs are present as crystallization substrates, $BaCO_3$ will selectively first nucleate on calcite, followed by aragonite, but not on vaterite for the same supersaturation levels. On the other hand, substrate solubility should favor the nucleation of $BaCO_3$ on vaterite over crystallization on aragonite, and least on calcite, due to significant local supersaturation occurring on the surfaces of the dissolving vaterite at low values of bulk carbonate content. The relative contributions of these two factors can be easily tuned by varying $[CO_3^{2-}]_{bulk}$, according to Eqs. 1-2. For high values of the $[CO_3^{2-}]_{bulk}$ the lattice mismatch is expected to dominate the crystallization position, whereas for low values of $[CO_3^{2-}]_{bulk}$ the solubility equilibrium of the substrate will increase the supersaturation in the vicinity of the least stable polymorphs.

These differences in lattice mismatches, in combination with external control over the local supersaturation allow us to selectively nucleate $BaCO_3$ on a predetermined polymorph of $CaCO_3$. To probe the influence of $[CO_3^{2-}]_{bulk}$, we developed a method to fabricate mixed polymorphic substrates containing all three polymorphs of $CaCO_3$ (typically, calcite 79±8%, aragonite 14±5% and vaterite 7±3%) by crystallizing $CaCO_3$ on an aluminum plate (see SI for details and setup). We vertically positioned the substrate containing all three $CaCO_3$ polymorphs in the reaction solution. As carbonate from the air entered the solution from the top, a $[CO_3^{2-}]$ gradient was created along the substrate, thus allowing for a continuous combinatorial screening of the influence of the $[CO_3^{2-}]_{bulk}$ on the overgrowth of the $CaCO_3$ polymorphs. To quantify the results, we manually counted each polymorph as a function of the depth (Fig. 2B). We define the polymorph overgrowth ratio $R_{Ba,x}$ for a specific $CaCO_3$ polymorph x as $R_{Ba,x} = (n_{Ba,x}/n_x)/\Sigma_{x'}(n_{Ba,x'}/n_{x'})$, with n_x denoting the total number of $CaCO_3$ crystals of a specific polymorph x; $n_{Ba,x}$ the number of $CaCO_3$ crystals of this polymorph that have been overgrown with $BaCO_3$, and the sum in the nominator running over all possible polymorphs (Fig. 2C). Additionally, we compute the cumulative distribution function (CDF) for each overgrown polymorph as a function of the depth in the solution (Fig. 2D).

Close to the meniscus (0.0-0.5 mm), the $[CO_3^{2-}]_{bulk}$ is the highest, which minimizes the effect of the local carbonate supersaturation due to polymorph dissolution. The lattice mismatch thus dominates the nucleation position, and $BaCO_3$ only nucleates on calcite and aragonite, with no nucleation on vaterite, which is expected as the lack of crystallographic alignment on vaterite results in a disadvantageous lattice mismatch. Deeper in the solution (0.5-2.0 mm), the lower $[CO_3^{2-}]_{bulk}$ decreases the local supersaturation around the calcite and aragonite crystals, and fewer of them become overgrown with $BaCO_3$. The lower $[CO_3^{2-}]_{bulk}$ also increases the dissolution of the least stable polymorph following Eq. 2, thus locally increasing the supersaturation around the vaterite crystals. Since the solubility of $BaCO_3$ is approximately tenfold lower than that of $CaCO_3$ polymorphs ($K_{sp\_BaCO3} << K_{sp\_CaCO3,x}$), the increase in CO_3^{2-} concentration around the dissolving vaterite crystals onsets the nucleation of $BaCO_3$. Below 2.0 mm $[CO_3^{2-}]_{bulk}$ the supersaturation is too low for nucleation on either calcite or aragonite crystals even though the lattice mismatch is favorable for these substrates. The stability-dependent dissolution completely dominates the nucleation and all vaterite crystals become overgrown. Dissolving vaterite crystals even increases the local CO_3^{2-} concentration to such an extent that crystallization of $BaCO_3$ may occur on an accidental calcite and aragonite crystal grown in close proximity to vaterite (Fig. SI 2B). It should be noted that a similar trend is found for the overgrowth of $CaCO_3$ polymorphs with $SrCO_3$ instead of $BaCO_3$ (Fig. SI 3), demonstrating that these principles can readily be extended to other systems. Furthermore, precise control over the spatial location and polymorphism of the $CaCO_3$ substrates may be gained using patterned self-assembled monolayers (11).

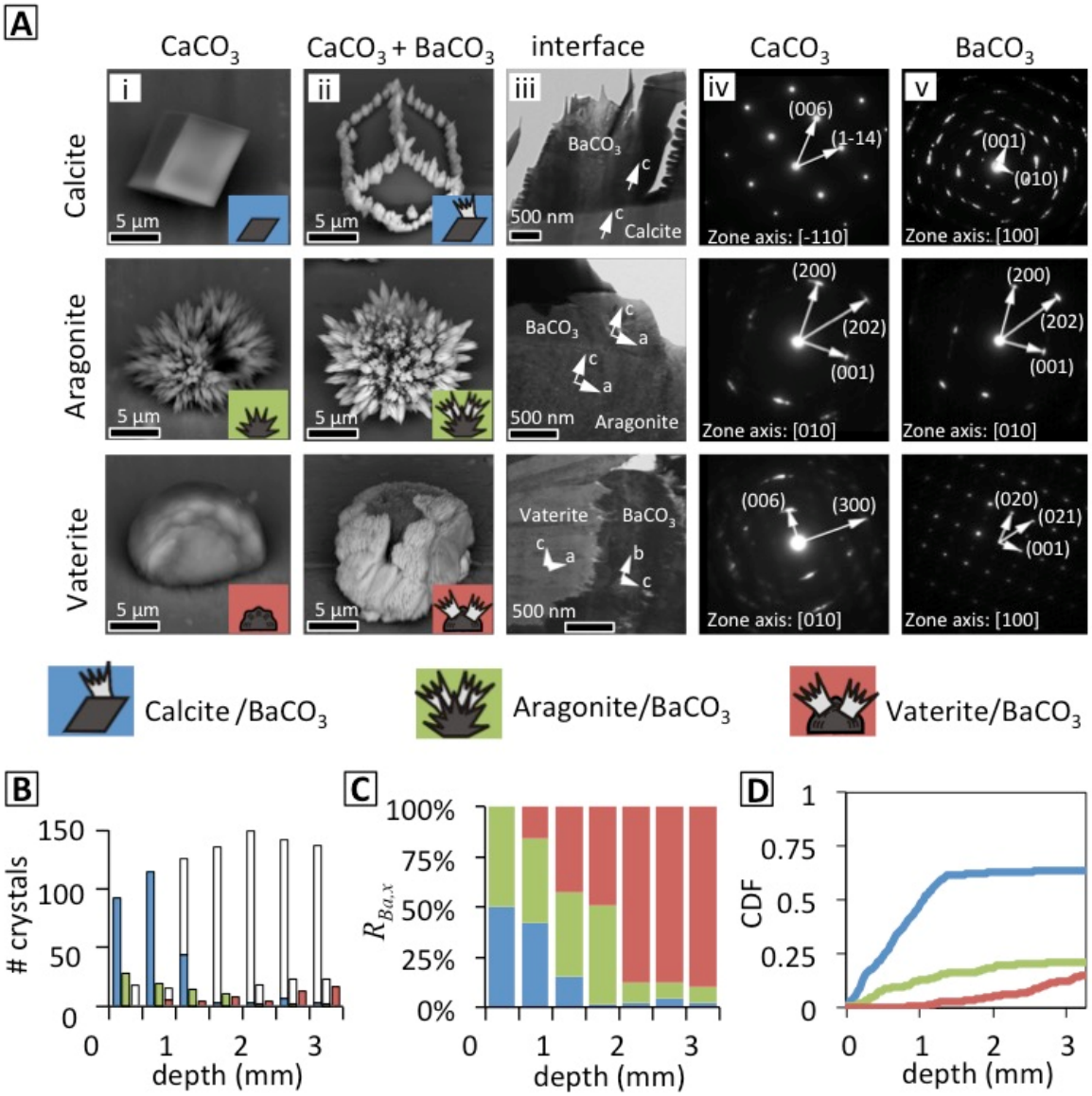

Fig. 2. Polymorph-selective nucleation of $BaCO_3$ on different $CaCO_3$ polymorphs. (A) Backscatter electron microscopy images were used to highlight the difference between $BaCO_3$ (appearing light) on different polymorphs of $CaCO_3$ (appearing dark). The lattice mismatches were estimated by measuring the crystallographic alignment of $BaCO_3$ on calcite, aragonite and vaterite (See SI). (ii) $BaCO_3$ crystals on top of the different polymorphs of $CaCO_3$. (iii-v) Transmission electron microscopic imaging and corresponding selected area electron diffraction at the interface revealed crystallographic alignment of two axes of $BaCO_3$ on top of both calcite and aragonite, whereas no crystallographic alignment was found on vaterite. (B-D) Three representations of statistical data of $CaCO_3$ overgrowth: (B) Total number of various polymorphs of $CaCO_3$ crystals as a function of depth: calcite (left bar), aragonite (middle bar) and vaterite (right bar). The number of the overgrown $CaCO_3$ crystals in each category are shown as filled bars: calcite-$BaCO_3$ (blue), aragonite-$BaCO_3$ (green) and vaterite-$BaCO_3$ (red); (C) Polymorph ratio based on data in figure 2B, highlighting that close to the meniscus $BaCO_3$ nucleation only occurs on calcite and aragonite, and deeper in the solution – only on vaterite; (D) Cumulative distribution function (CDF) of the overgrown crystals as a function of depth.

In order to create more complex shapes beyond the simple morphology of $BaCO_3$ crystals, we introduce silica to the reaction. The resulting $BaCO_3/SiO_2$ structures can straightforwardly be sculpted in a rich pallet of microshapes such as vases, spirals and corals by externally modulating

the reaction conditions, such as pH and temperature (28-31). The formation of these various shapes and their orientation is highly sensitive to and nearly fully determined by the concentrations of the reacting species in the vicinity of the developing structures, and can therefore act as an ideal model system to test the sensitivity of the nucleation events described above. Recently, we have also shown that precise control of the shape could lead to functional shapes such as those that can be used in photonics (31). In particular, by integrating a fluorescent dye as a light source in the nucleating barium carbonate seed crystal, effective waveguiding and beamsplitting through the rationally designed microarchitectures were achieved. While in this previous work no control over the position of these structures was obtained, the present study can introduce the ability to precisely control the location of the nucleation of these microstructures. Moreover, we anticipated that akin to chemotaxis, the creation of the local gradient in supersaturation induced by specific polymorphs of $CaCO_3$ placed in the immediate vicinity of the nucleating microstructures may be used to steer the growth of these structures in predetermined directions.

The precipitation of these $BaCO_3/SiO_2$ structures starts with the formation of a $BaCO_3$ crystal, which to a good approximation is not affected by the SiO_2. Hence we can assign the nucleation position in a manner analogous to how we directed the nucleation of $BaCO_3$ (Fig. 3A,B). Indeed, we find the same trend: preferred nucleation on calcite and aragonite at low immersion depths, whereas nucleation on vaterite only occurs deeper in the solution. Importantly, the ratio between the overgrown aragonite and calcite crystals in the top of the substrate gradually increases, with aragonite crystals being selectively overgrown at 0.75-1.5 mm (Fig. 3B), likely due to the growing contribution of the increase in local supersaturation from the dissolving calcium carbonate in the $BaCO_3$/aragonite system over the $BaCO_3$/calcite, as the bulk concentration in CO_2 goes down. It should be noted that the silica hampers the nucleation of $BaCO_3$. As a result, we observe a zone (2.0-5.0 mm) where the local supersaturation is insufficient to grow $BaCO_3/SiO_2$ structures and only below 5.0 mm is the local supersaturation sufficiently high to induce nucleation on vaterite. More complex shapes can be grown by rationally adjusting the reaction conditions, as exemplified by the $SrCO_3/SiO_2$ stems in Fig. 3C that were opened into vases using a CO_2 pulse and subsequently decorated with serrated edges using temperature modulations.

The ability to control nucleation on preselected polymorphs can also be used for positioning different materials on assigned polymorphs in sequential steps. We demonstrated this by first growing $CaCO_3$ spirals in the presence of polyaspartic acid (PAA) (32, 33). As these spirals are composed of vaterite nanocrystals, they selectively form on vaterite in the presence of all three polymorphs independent of the depth (Fig. 3D). With both the calcite and aragonite crystals still available, we subsequently positioned $BaCO_3/SiO_2$ spirals on the aragonite crystals while leaving the calcite crystals bare (Fig. 3E) at a depth of 1.5 mm.

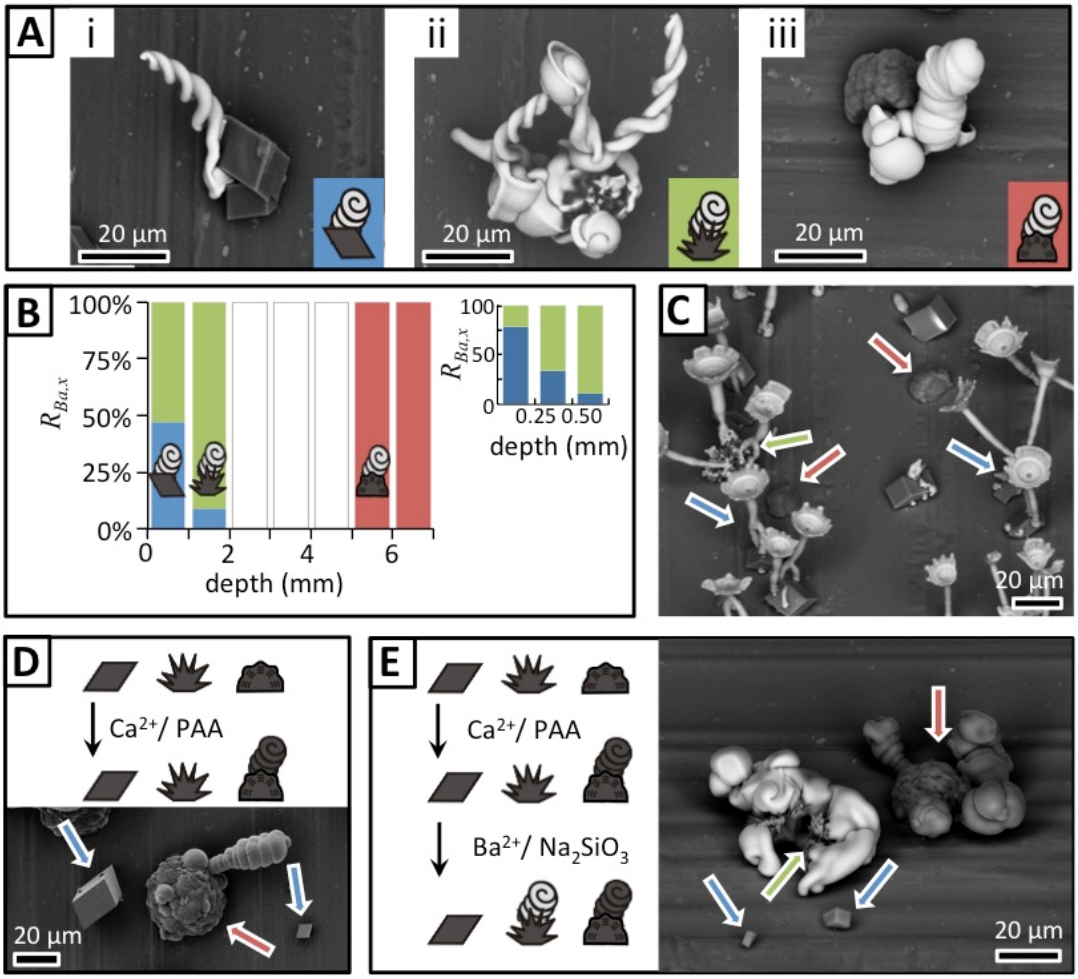

Fig. 3. Polymorph-selective nucleation of $BaCO_3/SiO_2$ and $CaCO_3$/PAA microstructures. (A) Backscatter scanning electron microscopy images of $BaCO_3/SiO_2$ grown on (i) calcite, (ii) aragonite and (iii) vaterite. (B) Polymorph ratio showing that $BaCO_3/SiO_2$ structures can selectively nucleate on $CaCO_3$ polymorphs by controlling the depth of immersion (see also SI). Inset at top right shows a more detailed polymorph ratio for the depth of 0-0.75 mm. (C) $SrCO_3/SiO_2$ stems that were opened into vases and decorated with serrated edges that selectively nucleated on calcite (blue arrow) and aragonite (green arrow) while vaterite (red arrow) is left empty. (D) $CaCO_3$/PAA spirals selectively nucleate on vaterite crystals. (E) Sequential nucleation steps can be used to first grow $CaCO_3$/PAA spirals (dark) on vaterite (dark) and subsequently place $BaCO_3$ spirals (light) on aragonite while leaving calcite empty.

Due the sensitivity of the $BaCO_3/SiO_2$ coprecipitation to local gradients, one can further define the growth direction of these sophisticated structures e.g. spirals, towards locally positioned carbonate sources. We ascertained this by growing $BaCO_3/SiO_2$ spirals on a substrate containing the mixture of $CaCO_3$ polymorphs at a depth of ca. 1.5 mm. According to Fig. 3B, at this depth the nucleation of $BaCO_3$ preferentially occurs on aragonite whereas neighboring vaterite gradually dissolves, thus causing a local increase in $[CO_3^{2-}]$ that could attract the growth front of the $BaCO_3/SiO_2$ structure and induce its directional chemotaxis. Indeed, we observed that $BaCO_3/SiO_2$ spirals first formed on aragonite, and subsequently grew only towards nearby dissolving vaterite, while not being influenced by neighboring calcite (Fig. 4). It should be noted that in the absence of silica, we also found that dissolving vaterite crystals could induce sufficient carbonate concentrations to induce nucleation on nearby calcite and vaterite crystals (Fig. SI 2B). Selectively lowering the relative energy barrier for nucleation on one polymorph and creating a

nearby local supersaturation by dissolving another polymorph thus provides simultaneous control over both the nucleation on preselected polymorphs and growth direction.

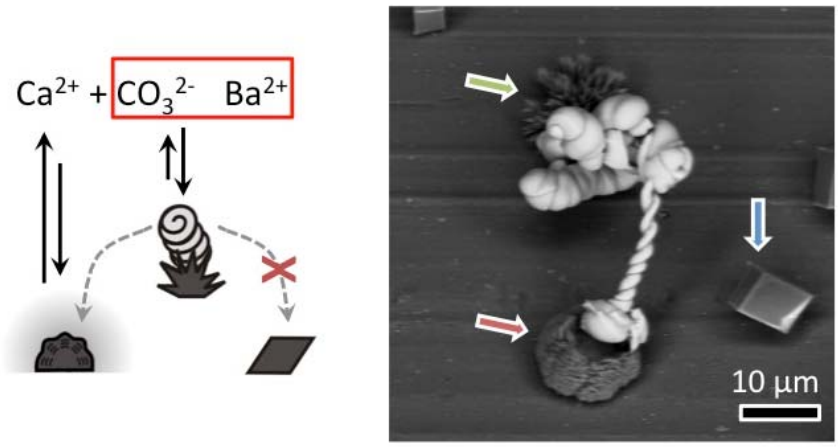

Fig. 4. Polymorph directed nucleation and growth. The balance between the local supersaturation and lattice mismatch can be controlled by the influx of CO_2 such that nucleation of a $BaCO_3/SiO_2$ microstructure first occurs at aragonite (green arrow) and subsequently grows towards nearby dissolving vaterite (red arrow) while leaving nearby calcite unaffected (blue arrow). The dotted arrow represents the direction of growth.

Summary and Conclusions

In conclusion, we have introduced a strategy to control the polymorph-specific positioning of mineralizing compounds and their directional growth using substrates with polymorphic mixtures as crystallization templates. The power of our approach is that merely the influx of carbonate allows us to manipulate the local concentrations of the crystallizing ions within a landscape of different interfacial energies. Therefore, by simultaneously controlling the concentration of carbonate from the bulk solution, the polymorph-dependent interfacial energy contribution from the lattice mismatch, and the substrate solubility, we are able to elicit unusual mineralization pathways unachievable by separate control over these individual parameters. In contrast with commonly used nucleation techniques that are based on lowering of the interfacial free energy only, we can therefore also nucleate selectively on substrates that have an unfavorable crystallographic alignment. Additionally, we can sequentially position different materials on assigned polymorphs and steer the growth of these structures in directions predetermined by the location of neighboring dissolving species. These concepts can perfect our ability to control nucleation and growth of nanostructured materials and may elucidate mechanisms that regulate nano- and microscale phenomena in biomineralization processes.

Methods

Crystallization of $CaCO_3$ polymorphic substrates. For the crystallization of mixed polymorphs of $CaCO_3$, 0.032 g of $CaCl_2$ was dissolved in 15 mL water in a 50 or 100 mL beaker. An aluminum slide (ca. 15x15x1 mm), or aluminum-coated microscope glass slide, was vertically positioned in the solution and the beaker was placed in a closed desiccator with freshly ground $(NH_4)_2CO_3$ following the method developed by Addadi *et al.* (6). After ca. 30-45 min, the slide was removed from the solution, washed twice with water and then washed with acetone and dried on the air. For details see SI Appendix, section 1.

Overgrowth of a $CaCO_3$ polymorph mixture with $BaCO_3$. In a 50 or 100 mL beaker, we dissolved 0.074 g $BaCl_2$ in 15 mL water and adjusted the pH to 11.9 using NaOH. A previously

prepared slide with a mixture of calcite, aragonite and vaterite (see above) was positioned at a 90º angle in the solution such that a half of the previously overgrown area (shown schematically as a green line in Fig. SI2A, left) was submerged. A petri dish was loosely placed on the beaker allowing for the CO_2 from the air to enter the beaker. After ca. 30-45 min, the slide was removed from the solution, washed twice with water and then washed with acetone and subsequently dried. Optical microscopy and SEM were used to analyze the slide and quantify the crystallization of the $BaCO_3$ on the $CaCO_3$ mixture. For details see SI Appendix section 2 and for overgrowth with $SrCO_3$ SI Appendix, section 3.

Overgrowth of a $CaCO_3$ polymorph mixture with $BaCO_3/SiO_2$ microstructures. In a 50 or 100 mL beaker, we dissolved 0.074 g of $BaCl_2$ and 0.016 g of Na_2SiO_3 in 15 mL water. To grow stem, vase and coral shaped structures, the pH was adjusted to pH 11.9 whereas for growth helices the pH was adjusted to 11.1 (30). A previously prepared slide with a mixture of calcite, aragonite and vaterite (see above) was positioned at 90º in the solution such that half of the previously overgrown area was submerged in the solution. A petri dish was loosely placed on the beaker such that CO_2 from the air could enter the beaker. After ca. 45 – 120 min, the slide was removed from the solution, washed twice with water and then washed with acetone and dried in the air. Optical microscopy and SEM were used to analyze the results.

Overgrowth of a $CaCO_3$ polymorph mixture with $CaCO_3$/PAA microstructures. In a 50 or 100 mL beaker, we dissolved 0.032 g of $CaCl_2$ and between 60 and 120 μg/mL poly (α,L-aspartate) (Sigma Aldrich) in 15 mL water. A previously prepared slide with a mixture of calcite, aragonite and vaterite (see above) was position under positioned at 90º in the solution such that half of the previously overgrown area was submerged. The beaker was placed in a closed desiccator with freshly ground $(NH_4)_2CO_3$ and placed in an oven at 45 °C. After ca. 45 – 120 min, the slide was removed from the solution, washed twice with water and then washed with acetone and dried in the air. Optical microscopy, Raman microscopy and SEM were used to analyze the slide.

FIB/TEM procedure. Samples were coated with Au (~5 nm) to reduce charging effects prior to focused ion beam (FIB) milling with a Helios Nanolab 660 Dual Beam electron microscope (FEI, OR). Typical TEM sample preparation procedure was as follows: 1) a platinum protective layer (~0.5 μm) was first laid down on top of the desired structure; 2) another platinum protective layer (~1.5 μm) was further deposited on top of the rectangular region where the TEM slab was to be milled out; 3) two sides of the coated structure, were milled away by FIB, leaving the slab of specimen (thickness: ~1.5 μm); 4) the slab was then cut through by FIB and transferred to a copper TEM grid by an Omniprobe and welded securely with platinum deposition; 5) the lift-out lamellar of specimen was sequentially thinned by FIB at 30, 16, 5, and 2 kV ion beam voltages. Final cleaning at 2 kV and 28 pA is important to obtain a clean surface and minimize damage. TEM imaging was carried out using a JEOL 2011 operated at 120 kV. For detailed section 6-8 in the SI Appendix for detailed figures, analysis of the crystal structure and calculation of the crystallographic mismatch.

Acknowledgements
Dr. Liesbeth Janssen and Prof Pieter Rein ter Wolde are kindly acknowledged for help with the manuscript. This research was supported by the NSF DMREF under award 15-33985 and the Harvard MRSEC under award DMR 14-20570. WLN thanks the Netherlands Organization for Scientific Research (NWO) for financial support from a VENI grant. LL thanks the Department of Mechanical Engineering at Virginia Tech for support. Electron microscopy and focused ion beam milling was performed at the Center for Nanoscale Systems at Harvard University,

supported by the NSF under award ECS-0335765, and at the Amsterdam nanoCenter, which was financially supported by NWO.

References

1. De Yoreo, J. J. *et al.* (2015) Crystallization by particle attachment in synthetic, biogenic, and geologic environments. *Science* **349**, 498.
2. Wegst, U. G. K., Bai, H., Saiz, E., Tomsia, A. P., Ritchie, R. O. (2014) Bioinspired structural materials. *Nature Mat.* **14**, 23-36.
3. Nielsen, M. H., Aloni, S., De Yoreo, J. J. (2014) In situ TEM imaging of $CaCO_3$ nucleation reveals coexistence of direct and indirect pathways. *Science* **345**, 1158-1162.
4. Smeets, P. J. M., Cho, K. R., Kempen, R. G. E., Sommerdijk, N. A. J. M., De Yoreo, J. J. (2015) Calcium carbonate nucleation driven by ion binding in a biomimetic matrix revealed by in situ electron microscopy. *Nature Mat.* **14**, 394–399.
5. Addadi, L. & Weiner, S. (1985) Interactions between acidic proteins and crystals: stereochemical requirements in biomineralization. *Proc. Natl. Acad. Sci.* **82**, 4110.
6. Addadi, L., Moradian, J., Shay, E., Maroudas, N. G., Weiner, S. (1987) A chemical model for the cooperation of sulfates and carboxylates in calcite crystal nucleation: Relevance to biomineralization. *Proc. Natl. Acad. Sci.* **84**, 2732-2736.
7. Heywood, B. R., Mann, S. (1994) Template-directed nucleation and growth of inorganic materials. *Adv. Mater.* **6**, 9-20.
8. Berman, A., Ahn, D. J., Lio, A., Salmeron, M., Reichert, A., Charych, D. (1995) Total alignment of calcite at acidic polydiacetylene films: cooperativity at the organic-inorganic interface. *Science* **259**, 515-518.
9. Litvin, A. L., Valiyaveettil, S., Kaplan, D. L., Mann, S. (1997) Template-directed synthesis of aragonite under supramolecular hydrogen-bonded langmuir monolayers. *Adv. Mater.* **9**, 124-127.
10. Aizenberg, J., Black, A. J., Whitesides, G. M. (1999) Control of crystal nucleation by patterned self-assembled monolayers. *Nature* **398**, 495-498.
11. Aizenberg, J. (2004) Crystallization in Patterns: A bio-inspired approach. *Adv. Mater.* **16**, 1295-1302.
12. Pokroy, B., Zolotoyabko, E. (2005) Aragonite growth on single-crystal substrates displaying a threefold axis. *Chem. Comm.* 2140-2142.
13. Gibbs, J. W. (1876) On the equilibrium of heterogeneous substances. *Trans. Connect. Acad. Sci.* **3,** 108-248.
14. Chernov, A. A. (1984). Modern Crystallography III: Crystal Growth. *Springer, Berlin* 978-3-642-81835-6.
15. De Yoreo, J. J., Vekilov, P. G., Dove, P.M., Weiner Eds, S. (2003) Principles of crystal nucleation and growth. In Biomineralization 57-93. *Mineral Soc. Am., Washington, DC* 10.2113/054005.
16. Bernstein, J. (2007) *Polymorphism in Molecular Crystals* (Oxford University Press, Oxford, UK).
17. Lowenstam, H. A., Weiner, S. (1989) *On Biomineralization* (Oxford University Press, Oxford, UK).
18. Mann, S., Ozin, G. A. (1996) Synthesis of inorganic materials with complex form. *Nature* **382**, 313.
19. Dove, P. M., Weiner, S., De Yoreo, J. J. (2003) Biomineralization. *Rev. Mineral. Geochem.* **54**.
20. Mann, S. (2001) *Biomineralization.* (Oxford University Press, Oxford, UK).
21. Sommerdijk, N. A. J. M., De With, G. (2008) Biomimetic $CaCO_3$ mineralization using designer molecules and interfaces. *Chem. Rev.* **108**, 4499–4550.

22. Kabalah-Amitai, L., Mayzel, B., Kauffmann, Y., Fitch, A. N., Bloch, L., Gilbert, P. U., Pokroy, B. (2013) Vaterite crystals contain two interspersed crystal structures. *Science* **340**, 454-457.
23. Kim, I. W., Robertson, R. E., Zand, R. (2003) Selected polymorphs of $CaCO_3$ through epitaxy with inorganic substrates aligned with an electric field. *Adv. Mater.* **15**, 709-712.
24. Plummer, L. N., Wigley, T. M. L., Parkhurst, D. L. (1978) The kinetics of calcite dissolution in CO_2 -water systems at 5 degrees to 60 degrees C and 0.0 to 1.0 atm CO_2. *Amer. J. Sci.* **278,** 179-216.
25. Chou, L., Garrels, R. M., Wollast, R. (1989) Comparative study of the kinetics and mechanisms of dissolution of carbonate minerals. *Chem. Geol,* **78,** 269-282.
26. Compton, R. G., Pritchard, K. L. (1990) The dissolution of calcite at pH > 7: kinetics and mechanism. *Phil. Trans. Roy. Soc. London,* **A330,** 47-70.
27. Inskeep, W. P., Bloom, P. R. (1985) An evaluation of rate equations for calcite precipitation kinetics at pCO_2 less than 0.01 atm and pH greater than 8. *Geochimica et Cosmochimica,* **49,** 2165-2180.
28. García-Ruiz, J. M., Amoros, J. L. (1981) Morphological aspects of some symmetrical aggregates grown by silica gel technique. *J. Cryst. Growth* **55**, 379-383.
29. García-Ruiz, J. M. *et al.* (2003) Self-assembled silica-carbonate structures and detection of ancient microfossils. *Science* **302**, 1194-1197.
30. Noorduin, W. L., Grinthal, A., Mahadevan, L., Aizenberg, J. (2013) Rationally designed complex, hierarchical microarchitectures. *Science* **340**, 832-837.
31. Kaplan, C. N. *et al.* (2017) Controlled growth and form of precipitating microstructures. *Science* **355**, 1395-1398.
32. Gower, L. A., Tirrell, D. A. (1998) Calcium carbonate films and helices grown in solutions of poly(aspartate). *J. Cryst. Growth* **191**, 153-160.
33. Sims, S. D., Didymus, J. M., Mann, S. (1995) Habit modification in synthetic crystals of aragonite and vaterite. *J. Chem. Soc., Chem. Comm.* **10**, 1031-1032.

Supplementary Information

Directed nucleation and growth by balancing local supersaturation and substrate/nucleus lattice mismatch

L. Li,[1,2,3] A. J. Fijneman,[1,4] J. A. Kaandorp,[5] J. Aizenberg,[1,2,6,7] W. L. Noorduin,[1,8]

[1]John A. Paulson School of Engineering and Applied Sciences, Harvard University, Cambridge, MA 02138, USA
[2]Wyss Institute for Biologically Inspired Engineering, Harvard University, Boston, MA 02115, USA
[3]Department of Mechanical Engineering, Virginia Polytechnic Institute and State University, Blacksburg, VA 24060, USA
[4]Department of Chemical Engineering and Chemistry, Eindhoven University of Technology, 5612 AZ Eindhoven, The Netherlands
[5]Computational Science Lab, Faculty of Science, University of Amsterdam, 1098 XH Amsterdam, The Netherlands
[6]Kavli Institute for Bionano Science and Technology, Harvard University, Cambridge, MA 02138, USA
[7]Department of Chemistry and Chemical Biology, Harvard University, Cambridge, MA 02138, USA
[8]AMOLF, 1098 XG Amsterdam, The Netherlands.

Content

1. Simultaneous crystallization of calcite, aragonite, and vaterite

For the crystallization of mixed polymorphs of $CaCO_3$, 0.032 g of $CaCl_2$ was dissolved in 15 mL water in a 50 or 100 mL beaker. An aluminum slide (ca. 15x15x1 mm), or aluminum-coated microscope glass slide, was vertically positioned in the solution and the beaker was placed in a closed desiccator with freshly ground $(NH_4)_2CO_3$ following the method developed by Addadi *et al.* (*1*). After ca. 30-45 min, the slide was removed from the solution, washed twice with water and then washed with acetone and dried on the air. Optical microscopy, scanning electron microscopy (SEM) and Raman microscopy revealed that the slide contained a mixture of calcite (79±8%), aragonite (14±5%) and vaterite (7±3%) (Fig. SI 1).

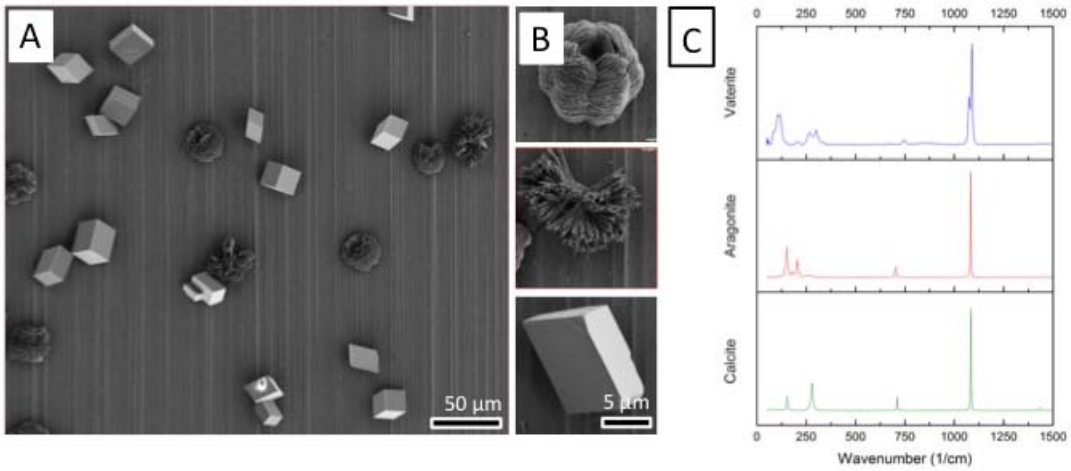

Figure SI 1. Crystallization of calcite, aragonite and vaterite. (A) SEM image of a typical sample area containing a mixture of vaterite, aragonite and calcite. (B) Close up SEM images of vaterite, aragonite and calcite (top to bottom). (C) Raman spectra absorption spectra of vaterite, aragonite and calcite crystals excited at 514 nm.

2. Overgrowth of a $CaCO_3$ polymorph mixture with $BaCO_3$

In a 50 or 100 mL beaker, we dissolved 0.074 g $BaCl_2$ in 15 mL water and adjusted the pH to 11.9 using NaOH. A previously prepared slide with a mixture of calcite, aragonite and vaterite (see above) was positioned at a 90º angle in the solution such that a half of the previously overgrown area (shown schematically as a green line in Fig. SI2A, left) was submerged. A petri dish was loosely placed on the beaker allowing for the CO_2 from the air to enter the beaker. After ca. 30-45 min, the slide was removed from the solution, washed twice with water and then washed with acetone and subsequently dried. Optical microscopy and SEM were used to analyze the slide and quantify the crystallization of the $BaCO_3$ on the $CaCO_3$ mixture (shown schematically as a red line in Fig. SI 2A, left). To quantify the polymorphic overgrowth, we manually counted each polymorph as a function of the depth. Subsequently we plotted the cumulative distribution function. Alternatively, we define the polymorph overgrowth ratio $R_{Ba,x}$ for a specific $CaCO_3$ polymorph x as $R_{Ba,x} = (n_{Ba,x}/n_x)/\Sigma_{x'}(n_{Ba,x'}/n_{x'})$, with n_x denoting the total number of $CaCO_3$ crystals of the polymorph, $n_{Ba,x}$ the number of $CaCO_3$ crystals of this polymorph that have been overgrown with $BaCO_3$, and the sum in the nominator running over all possible polymorphs.

The CDF is computed by manually counting the overgrown $CaCO_3$ crystals per polymorph as a function of the depth as a fraction of the total number of overgrown $CaCO_3$ crystals. Note that the CDF does not include the data of the $CaCO_3$ crystals that are not overgrown.

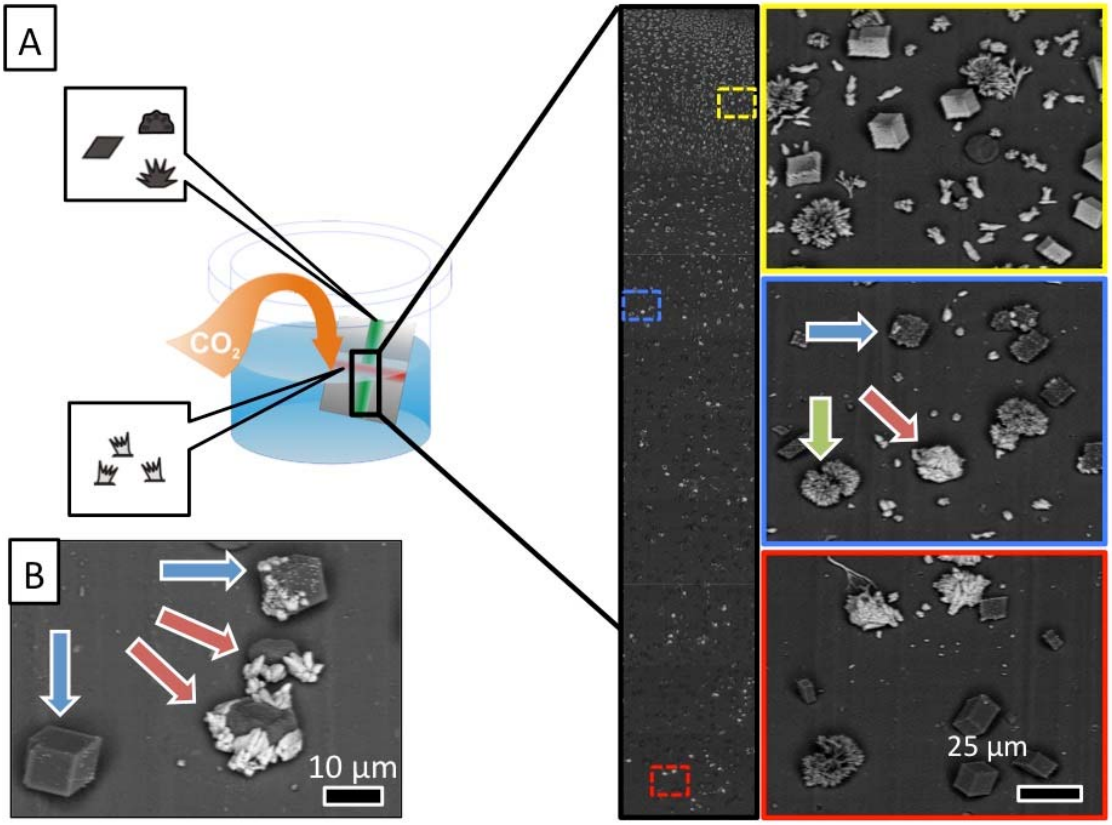

Figure SI 2. Analysis of overgrowth of a $CaCO_3$ polymorph mixture with $BaCO_3$. (A) Left: Schematic drawing showing the positioning of the substrate containing the mixture of $CaCO_3$ polymorphs (green line and the inset on the top) that becomes overgrown with $BaCO_3$ (red line and the lower inset). Right: Backscatter SEM images, in which $BaCO_3$ appears light and $CaCO_3$ appears dark, qualitatively show that at the top (yellow box) calcite and aragonite are overgrown, deeper in the solution (blue box) all three polymorphs are overgrown and at the deepest part (red box) mainly vaterite crystals are overgrown. (B) Backscatter SEM image taken at the deepest part in the solution (2.5-3.0mm) showing two overgrown vaterite crystals (red arrow). The local increase in the $[CO_3^{2-}]$ from the dissolving vaterite crystals also caused crystallization on a calcite crystal that grew in the immediate vicinity of vaterite; note that the overgrowth of $BaCO_3$ on this crystal takes place on the surface facing the nearby vaterite (top blue arrow), whereas a calcite crystal further away from the vaterite crystals remains empty (bottom blue arrow).

3. Overgrowth of a $CaCO_3$ polymorph mixture with $SrCO_3$

In a 50 or 100 mL beaker we dissolved 0.084 g of $SrCl_2$ in 15 mL water and adjusted the pH to 11.9 using NaOH. A similar procedure was followed as for $BaCO_3$ as described above. Optical microscopy and SEM were used to analyze the results and quantify the crystallization of the $SrCO_3$ on the $CaCO_3$ mixture (Fig. SI 3).

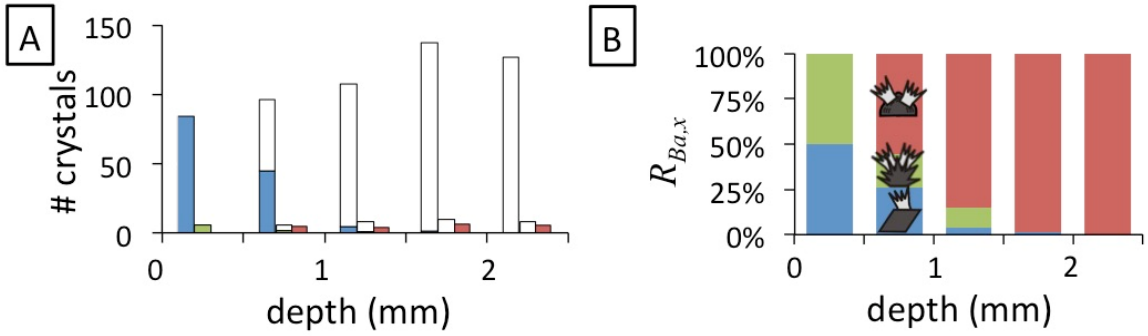

Figure SI 3. Analysis of overgrowth of a $CaCO_3$ polymorph mixture with $SrCO_3$. (A) Number of $CaCO_3$ crystals as a function of the depth: calcite (left clear bar), aragonite (middle clear bar) and vaterite (right clear bar), and number of overgrown $CaCO_3$ crystals: calcite-$SrCO_3$ (left blue bar), aragonite-$SrCO_3$ (middle green bar) and vaterite-$SrCO_3$ (right red bar). (B) Polymorph overgrowth ratio $R_{Ba,x}$ based on data in Fig. SI 3A.

4. Overgrowth of a $CaCO_3$ polymorph mixture with $BaCO_3/SiO_2$ microstructures

In a 50 or 100 mL beaker, we dissolved 0.074 g of $BaCl_2$ and 0.016 g of Na_2SiO_3 in 15 mL water. To grow structures in the blossoming regime, the pH was adjusted to pH 11.9 whereas for growth in the curling regime the pH was adjusted to 11.1 (*2*). A previously prepared slide with a mixture of calcite, aragonite and vaterite (see above) was positioned at 90º in the solution such that half of the previously overgrown area was submerged in the solution. A petri dish was loosely placed on the beaker such that CO_2 from the air could enter the beaker. After ca. 45 – 120 min, the slide was removed from the solution, washed twice with water and then washed with acetone and dried in the air. Optical microscopy and SEM were used to analyze the results.

5. Overgrowth of a $CaCO_3$ polymorph mixture with $CaCO_3$/PAA microstructures

In a 50 or 100 mL beaker, we dissolved 0.032 g of $CaCl_2$ and between 60 and 120 µg/mL poly (α,L-aspartate) (Sigma Aldrich) in 15 mL water. A previously prepared slide with a mixture of calcite, aragonite and vaterite (see above) was position under positioned at 90º in the solution such that half of the previously overgrown area was submerged. The beaker was placed in a closed desiccator with freshly ground $(NH_4)_2CO_3$ and placed in an oven at 45 °C. After ca. 45 – 120 min, the slide was removed from the solution, washed twice with water and then washed with acetone and dried in the air. Optical microscopy, Raman microscopy and SEM were used to analyze the slide.

6. FIB/TEM procedure

Samples were coated with Au (~5 nm) to reduce charging effects prior to focused ion beam (FIB) milling with a Helios Nanolab 660 Dual Beam electron microscope (FEI, OR). Typical TEM sample preparation procedure was as follows: 1) a platinum protective layer (~0.5 µm) was first laid down on top of the desired structure; 2) another platinum protective layer (~1.5 µm) was further deposited on top of the rectangular region where the TEM slab was to be milled out; 3) two sides of the coated structure, were milled away by FIB, leaving the slab of specimen (thickness: ~1.5 µm); 4) the slab was then cut through by FIB and transferred to a copper TEM grid by an Omniprobe and welded securely with platinum deposition; 5) the lift-out lamellar of specimen was

sequentially thinned by FIB at 30, 16, 5, and 2 kV ion beam voltages. Final cleaning at 2 kV and 28 pA is important to obtain a clean surface and minimize damage. TEM imaging was carried out using a JEOL 2011 operated at 120 kV.

7. Crystal structure Analysis

Table SI 1: Crystallographic information for various $CaCO_3$ polymorphs, $BaCO_3$ and $SrCO_3$.

Substance	Polymorph (Common name)	Crystal system	Space group	a/Å	b/Å	c/Å	α/(°)	β/(°)	γ/(°)
$CaCO_3$	Calcite	Trigonal	$R\bar{3}c$	4.988	4.988	17.061	90	90	120
	Aragonite	Orthorhombic	Pmcn	4.961	7.967	5.741	90	90	90
	Vaterite	Hexagonal	P63/mmc	7.290	7.290	25.302	90	90	120
$BaCO_3$	Witherite	Orthorhombic	Pmcn	5.313	8.896	6.428	90	90	90
$SrCO_3$	Strontianite	Orthorhombic	Pmcn	5.090	8.358	5.997	90	90	90

Calcite/$BaCO_3$

Based on TEM/diffraction studies (Fig. 2 and Fig. SI 4), the *c*-axes of the two types of crystals are aligned. Diffraction results also suggest that the $(10\bar{1}0)$ planes of calcite are aligned with (010) planes of $BaCO_3$. Although it was not explicitly stated, similar diffraction results were obtained by Wu *et al.* (*3, 4*) for the cases of Ca-doped $SrCO_3$ and $BaCO_3$ on the substrate of calcite, respectively.

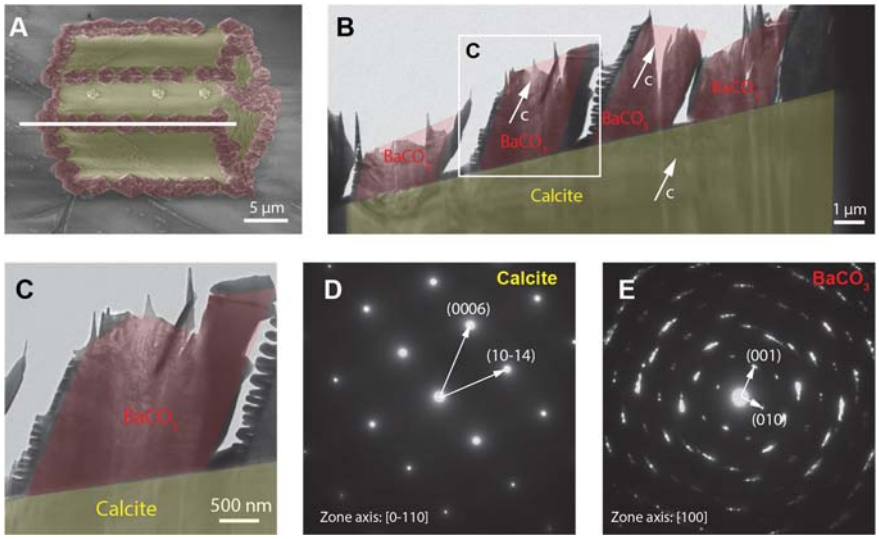

Fig. SI 4. Structural analysis of calcite/$BaCO_3$ interface. (A) Top-view SEM image of the original calcite crystal overgrown with $BaCO_3$ crystals. The white line indicates the location and orientation of the TEM sample prepared via FIB milling. (B) Overview TEM image of the overgrowth of multiple $BaCO_3$ crystals (red regions) on calcite (yellow region). The top portions of $BaCO_3$ crystals were milled away during FIB polishing. (C) A representative TEM image of $BaCO_3$/calcite interface. Selected area electron diffraction patterns of underlying calcite substrate and overgrown $BaCO_3$ crystal acquired from regions in (C).

Aragonite/$BaCO_3$

TEM analysis showed that the crystallographic axes of $BaCO_3$ and aragonite are aligned (Fig. 2 and Fig. SI 5).

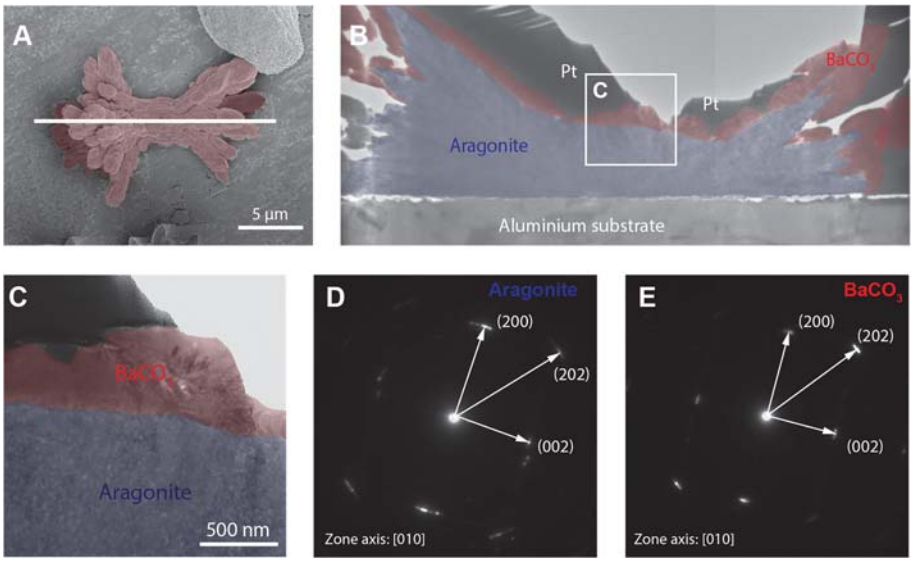

Fig. SI 5. Structural analysis of aragonite/$BaCO_3$ interface. (A) Top-view SEM image of the original aragonite crystal overgrown with $BaCO_3$ crystals. The white line indicates the location and orientation of the TEM sample prepared via FIB milling. (B) Overview TEM image of the overgrowth of $BaCO_3$ crystals (red regions) on aragonite (blue region). (C) A representative TEM image of $BaCO_3$/aragonite interface. Selected area electron diffraction patterns of underlying aragonite substrate and overgrown $BaCO_3$ crystal acquired from regions in (C).

<u>Vaterite/$BaCO_3$</u>

The vaterite crystals have their *c*-axis perpendicular to the microplates and the *a*-axis is parallel to the growth direction as shown in the hexagonal-shaped crystal used for TEM imaging shown in Fig. 2A, column iv and Fig. SI 6. This has been observed in a previous report (*5*). Electron diffraction studies in multiple locations at the vaterite/$BaCO_3$ interface do not show a consistent correlation for the crystal orientations in vaterite and $BaCO_3$.

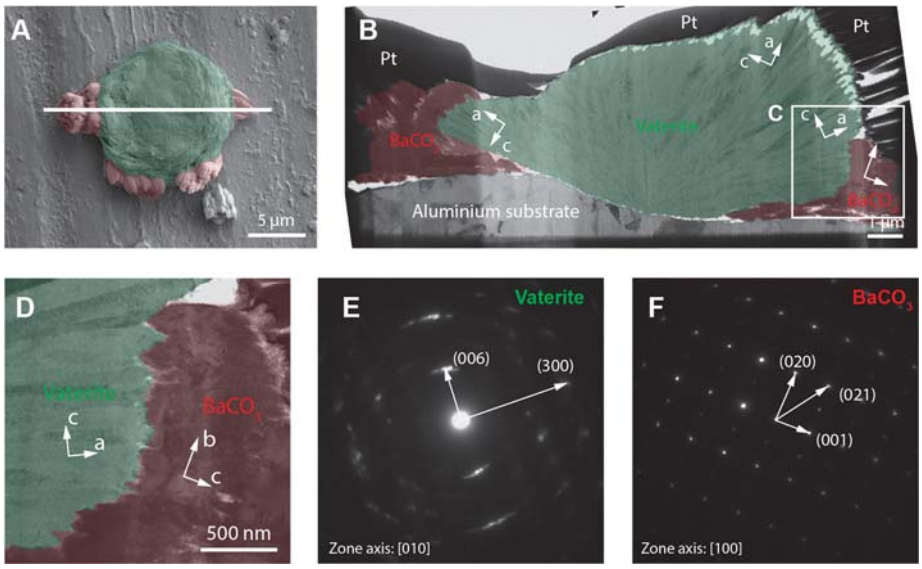

Fig. SI 6. Structural analysis of vaterite/$BaCO_3$ interface. (A) Top-view SEM image of the original vaterite crystal overgrown with $BaCO_3$ crystals. The white line indicates the location and orientation of the TEM sample prepared via FIB milling. (B) Overview TEM image of the

overgrowth of $BaCO_3$ crystals (red regions) on vaterite (blue region). (C) A representative TEM image of $BaCO_3$/vaterite interface. Selected area electron diffraction patterns of vaterite and overgrown $BaCO_3$ crystals acquired from regions in (C).

8. Calculations of crystal lattice mismatch

Based on the structural analysis in the previous session, we are able to determine the lattice mismatch between overgrowth crystals ($BaCO_3$ and $SrCO_3$) and different $CaCO_3$ polymorph crystals (calcite and aragonite) as substrates (**Fig. SI 7**). Here we adopt a similar approach reported by Pokroy and Zolotoyabko (*6*) in estimating lattice mismatches in both ***a*** and ***b*** directions. For the case of aragonite as a substrate, the mismatch M^a and M^b can be calculated according to the equations below

$$M^a = \frac{a_{overgrowth} - a_{substrate}}{a_{substrate}}$$

and

$$M^b = \frac{b_{overgrowth} - b_{substrate}}{b_{substrate}}$$

The average lattice mismatch is defined as

$$|\bar{M}| = (|M^a| + |M^b|)/2$$

For the case of calcite as a substrate, which is a rhombohedral crystal, the equivalent ***b**** of the orthorhombic unit cell (**Fig. SI 5**) is

$$b^* = \sqrt{3}a$$

Then the lattice mismatch can be calculated by using the same relationships above by replacing ***b*** with ***b****.

The calculated mismatch values are tabulated in **Table SI 2**. It is noted that for both overgrowth of $BaCO_3$ and $SrCO_3$, the lattice mismatch in both ***a*** and ***b*** directions is slightly smaller for the case of calcite as the substrate in comparison to the case of aragonite as the substrate.

Table SI 2: Crystal lattice mismatch between substrate (calcite and aragonite) and overgrowth ($BaCO_3$ and $SrCO_3$) crystals. The relevant parameters are defined in the text.

Type	Substance	Crystal system	a/Å	b/Å	b*/Å	Calcite as substrate			Aragonite as substrate		
						M^a	M^b	$\|\bar{M}\|$	M^a	M^b	$\|\bar{M}\|$
Substrate	**Calcite**	Trigonal	4.988	4.988	8.6395						
	Aragonite	Orthorhombic	4.961	7.967	7.967						
Overgrowth	**$BaCO_3$**	Orthorhombic	5.313	8.896	8.896	0.0652	0.0297	**0.0474**	0.0710	0.1166	**0.0938**
	$SrCO_3$	Orthorhombic	5.090	8.358	8.358	0.0204	0.0326	**0.0265**	0.0260	0.0491	**0.0375**

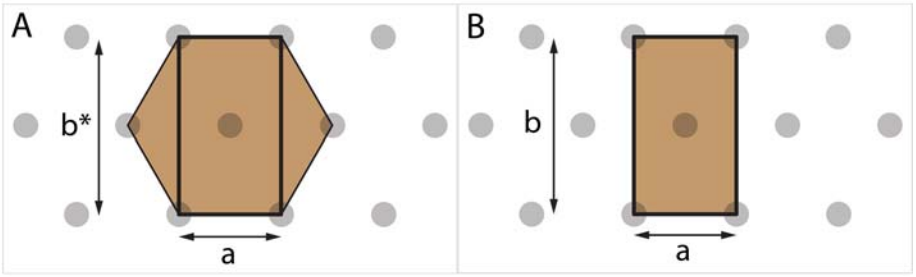

Fig. SI 7. Schematic diagram of cation (indicated by the gray dots) arrangement in the (001) plane of rhombohedral (calcite) and orthorhombic (aragonite, $BaCO_3$ and $SrCO_3$) crystals. Note for the case calcite as substrate, the $(10\bar{1}0)$ planes of calcite are aligned with (010) planes of $BaCO_3$, as observed from the TEM and electron diffractions.

9. Derivation of equation 2

For the derivation of equation 2, we start by defining a rate equation for the local carbonate concentration $[CO_3^{2-}]_{local}$ from the dissolution of the different calcium carbonate polymorphs $CaCO_{3x}$. According to Plummer *et al.* (*7,8*) the dissolution rate v_{net} of $CaCO_3$ can be described as:

$$v_{net} = k_1 a_{H^+} + k_1 a_{HCO_3^-} + k_3 a_{H_2O} - k_4 a_{Ca^{2+}} a_{HCO_3^-} \quad (1)$$

where a_x denotes the bulk solution activity of species x and k_1, k_2, k_3, and k_4 are rate constants. A modified version of the Plummer *et al.* model also contains the dissolution/precipitation of calcite and aragonite (*9,10*). According to this modified model the dissolution of calcite in three regions of pH is controlled by the following reactions:

$$\begin{aligned} &CaCO_3 + H^+ \rightleftarrows HCO_3^- \\ &CaCO_3 + H_2CO_3 \rightleftarrows Ca^{2+} + 2HCO_3^- \\ &CaCO_3 \rightleftarrows Ca^{2+} + CO_3^{2-} \end{aligned} \quad (2)$$

For pH > 7 a rate reaction equation was derived from the Plummer model describing the dissolution rate (*10-12*):

$$v_{net} = k_x - k_x'[Ca^{2+}]_s[CO_3^{2-}]_s \quad (3)$$

where $k_x' = k_x/K_{sp\text{-}CaCO3x}$ with the solubility product $K_{sp\text{-}CaCO3x}$, and k_x is the dissolution rate constant of $CaCO_3$ which depends on the surface morphology of the dissolving crystal and on the specific polymorph x. The subscript s denotes the concentrations in the surface layers near the dissolving calcium carbonate crystal. The values for k_x' and k_x correspond to the values of k_3 and k_4 in the Plummer model. When we use k_x in equation 3 for the specific polymorphs of calcium carbonate, then we can assume $k_{vaterite} > k_{aragonite} > k_{calcite}$ and $K_{sp,vaterite} > K_{sp,aragonite} > K_{sp,calcite}$. Please note that for the regime we consider the dissolution rate is positive, i.e. $k_x > k_x/K_{sp\text{-}CaCO3x}[Ca^{2+}][CO_3^{2-}]$.

Using this expression for the dissolution rate of calcium carbonate, we can now formulated the local concentration of CO_3^{2-} in time during the nucleation of $BaCO_3$, while the underlying $CaCO_3$ crystal is dissolving and additional influx of CO_3^{2-} occurs from the bulk solution. When we assume that the contribution of reverse reactions is very

small and we do not consider diffusion, the rate equation for the carbonate concentration around the nucleating $BaCO_3$ crystal $[CO_3^{2-}]_{local}$ can be expressed as:

$$\frac{d[CO_3^{2-}]_{local}}{dt} = k_{\inf lux}[CO_3^{2-}]_{bulk} + k_x - k_x^{'}[Ca^{2+}]_s[CO_3^{2-}]_s - k_{BaCO_3}[Ba^{2+}][CO_3^{2-}]_{local} \quad (4)$$

where k_{influx} is a rate constant describing the influx of CO_3^{2-} from the bulk solution towards the nucleating $BaCO_3$ crystal, and k_{BaCO3} the crystallization rate constant.
The dissolution term for $CaCO_{3,x}$ is described by equation (3). Since the growth of the crystal is relatively slow compared to the diffusion of $[CO_3^{2-}]_{local}$, we can assume a steady state in $[CO_3^{2-}]_{local}$:

$$\frac{d[CO_3^{2-}]_{local}}{dt} = 0 \quad (5)$$

Furthermore, we can assume $[CO_3^{2-}]_{local} = [CO_3^{2-}]_s$ since nucleation of $BaCO_3$ occurs on the surface of the $CaCO_3$, such that equation (4) changes into:

$$k_{\inf lux}[CO_3^{2-}]_{bulk} = -k_x + k_x^{'}[Ca^{2+}]_s[CO_3^{2-}]_{local} + k_{BaCO_3}[Ba^{2+}][CO_3^{2-}]_{local} \quad (6)$$

$$\frac{k_{\inf lux}[CO_3^{2-}]_{bulk}}{[CO_3^{2-}]_{local}} = k_{BaCO_3}[Ba^{2+}] - k_x + k_x^{'}[Ca^{2+}]_s \quad (7)$$

$$[CO_3^{2-}]_{local} = \frac{k_{\inf lux}[CO_3^{2-}]_{bulk}}{k_{BaCO_3}[Ba^{2+}] - k_x + k_x^{'}[Ca^{2+}]_s} \quad (8)$$

with k_{BaCO3} the crystallization rate constant of $BaCO_3$. The formation of $BaCO_3$ under supersaturated conditions is described by:

$$\frac{d[BaCO_3]}{dt} = k_{BaCO_3}[Ba^{2+}][CO_3^{2-}]_{local} \quad (9)$$

Substitution of (8) into (9) gives:

$$\frac{d[BaCO_3]}{dt} = \frac{k_{BaCO_3}[Ba^{2+}]k_{\inf lux}[CO_3^{2-}]_{bulk}}{k_{BaCO_3}[Ba^{2+}] - k_x + k_x^{'}[Ca^{2+}]_s} \quad (10)$$

The free energy of the solution per molecule is (*13,14*):

$$\Delta g_{sol} = -k_B T \ln K_{sp-BaCO_3} \quad (11)$$

The change in chemical potential is given by (*13,14*):

$$\Delta\mu = k_B T \ln\left(\frac{[Ba^{2+}][CO_3^{2-}]_{local}}{K_{sp-BaCO_3}}\right) \quad (12)$$

and the supersaturation σ can be written as:

$$\sigma = \ln(\frac{[Ba^{2+}][CO_3^{2-}]_{local}}{K_{sp-BaCO_3}}) \quad (13)$$

where k_B is the Boltzmann constant, K_{sp_BaCO3} is the solubility product of $BaCO_3$ and T is the absolute temperature.

Since $[CO_3^{2-}]_{local}$ depends on $[CO_3^{2-}]_{bulk}$, $[Ba^{2+}]$, and $[Ca^{2+}]$s (see Eq. 8), it is useful to substitute Eq. 8 into Eq. 13 and set k_{influx} to unity. Furthermore, we use the relation for the equilibrium constant K_c,:

$K_c = \frac{k_{BaCO_3}}{k_-} = \frac{[BaCO_3]_{eq}}{[Ba^{2+}]_{eq}[CO_3^{2-}]_{eq}}$, with k_- the dissolution rate constant of $BaCO_3$. By substituting $K_{sp\_BaCO_3} = [Ba^{2+}]_{eq}[CO_3^{2-}]_{eq}$ and setting the activity of the solid $[BaCO_3]_{eq}$ and k_- to unity leads to: $K_{sp-BaCO_3} \approx \frac{1}{k_{BaCO_3}}$, such that the supersaturation can be written as:

$$\sigma = \ln\left(\frac{k_{BaCO_3}[Ba^{2+}][CO_3^{2-}]_{bulk}}{k_{BaCO_3}[Ba^{2+}] - k_x + k_x'[Ca^{2+}]_s}\right). \quad (14)$$

References

1. L. Addadi, J. Moradian, E. Shay, N. G. Maroudas, S. Weiner, *Proc. Natl. Acad. Sci.* ***84,*** 2732-2736 (1987).
2. W.L. Noorduin, A. Grinthal, L. Mahadevan, J. Aizenberg, *Science* ***340,*** 832-837 (2013).
3. W. Wu, Y. Ma, Y. Xing, Y. Zhang, H. Yang, Q. Luo, J. Wang, B. Li, L. Qi, *Cryst. Growth Des.* ***15,*** 2156-2164 (2015).
4. W. Wu, Y. Zhang, B. Li, Y. Ma, *Acta Phys. –Chim. Sin.* ***31***, 189-198 (2015).
5. Q. Hu, J. Zhang, H. Teng, U. Becker, *Amer. Miner.* ***97,*** 1437–1445 (2012).
6. B. Pokroy and E. Zolotoyabko, *Chem. Comm.* 2140-2142 (2005).
7. L.N. Plummer, D.L. Parkhurst, T.M.L. Wigley, *ACS Symposium Series****, 93,*** 537-573 (1979).
8. L.N. Plummer, T.M.L. Wigley, D.L. Parkhurst, *Amer. J. Sci.* ***278,*** 179-216 (1978).
9. L. Chou, R.M. Garrels, R. Wollast, *Chem. Geol.* ***78,*** 269-282 (1989).
10. R.G. Compton, K.L. Pritchard, *Phil. Trans. Roy. Soc. London,* ***A330,*** 47-70 (1990).
11. W.P. Inskeep and P.R. Bloom, *Geochimica et Cosmochimica,* ***49,*** 2165-2180, (1985).
12. B. Sanjuan, J.P. Girard, *Review of kinetic data on carbonate mineral precipitation*, *BRGM Report R39062*, 1-91 (1996).
13. A.A. Chernov, (1984). Modern Crystallography III: Crystal Growth. *Springer, Berlin* 978-3-642-81835-6.
14. J.J. De Yoreo, P.G Vekilov, P. M. Dove, Weiner Eds, S. (2003) Principles of crystal nucleation and growth. In Biomineralization 57-93. *Mineral Soc. Am., Washington, DC* 10.2113/054005.